energies

MDPI

Article

A Hybrid Analytical Model for the Electromagnetic Analysis of Surface-Mounted Permanent-Magnet Machines Considering Stator Saturation

Wenbiao Lu [1], Jie Zhu [1], Youtong Fang [1,2] and Pierre-Daniel Pfister [1,2,*]

[1] College of Electrical Engineering, Zhejiang University, Hangzhou 310027, China
[2] Zhejiang Provincial Key Laboratory of Electrical Machine Systems, Zhejiang University, Hangzhou 310027, China
* Correspondence: pierredaniel.pfister.public@gmail.com

Abstract: This article presents the process of building a hybrid analytical model (HAM) for surface-mounted permanent-magnet machines. The HAM couples a reluctance network (RN) model in the stator region with a magnetic scalar potential analytical model in the air gap and magnets regions. This hybrid model can deal with the slotting effect with straight teeth, and takes magnetic saturation into account in the stator iron material using the RN model. It is calculated under open-circuit and loaded conditions. The magnetic flux density, flux linkage, back electromotive force (EMF), and torque of the machines are also calculated. This hybrid model is compared with the subdomain method. It is also compared with the finite element method (FEM) both in terms of the size of the matrix that needs to be calculated and in terms of the torque error. We analyzed this method for two surface-mounted permanent-magnet machines, one with a symmetry factor of four and another with a symmetry factor of three. In both cases, HAM reduced the size of the matrix that needed to be solved compared to FEM. In the machine with a symmetry factor of three, when the matrix size of both FEM and HAM was around 1700 × 1700, the torque error of FEM was 2.62% compared to the high-mesh-density FEM simulation, while the torque error of HAM was only 0.17% compared to the same simulation. HAM also had significant advantages over the subdomain method, as it reduced the torque error from 16.8% to 0.08% in the case of high magnetic saturation. The HAM can, hence, play a significant role in the design and optimization of surface-mounted permanent-magnet machines, especially in cases where magnetic saturation is present.

Keywords: hybrid model; permanent-magnet machine; reluctance network; analytical model; magnetic saturation

Citation: Lu, W.; Zhu, J.; Fang, Y.; Pfister, P.-D. A Hybrid Analytical Model for the Electromagnetic Analysis of Surface-Mounted Permanent- Magnet Machines Considering Stator Saturation. *Energies* **2023**, *16*, 1300. https://doi.org/10.3390/en16031300

Academic Editors: Mauro Andriollo and Andrea Tortella

Received: 5 December 2022
Revised: 3 January 2023
Accepted: 19 January 2023
Published: 26 January 2023

1. Introduction

Much research has been performed on efficient and accurate modeling approaches of magnetic fields for different types of electrical machine topologies. Those approaches can mainly be divided into numerical and analytical.

1.1. Numerical Methods

With the variety in commercial software, the finite element method (FEM) provides a convenient way to perform simulations and obtain precise results. It is, hence, widely used for analyzing the electromagnetic performance of machines. However, it requires high computational time due to the meshing of the geometry. When many geometrical parameters need to be optimized at the initial stage of designing a machine, the time consumption can be prohibitive [1].

Another numerical technique is the reluctance network (RN). One way to build the network is on the basis of the predicted probable magnetic flux path [2,3]. In practice, flux paths change due to saturation, and paths in small areas are often uncertain and overlooked.

Moreover, in many models, flux paths in the air gap are assumed to only be in the radial direction, and the circumferential fluxes are neglected. All these shortcomings determine the inaccuracy of this model.

Another way to build an RN is to mesh the machine into small regular elements, each node being connected by a magnetic reluctance. This does not require predicting flux paths. This method has the advantage that, if multiple simulations are needed as a function of the rotor position, the same reluctance network can be used [4]. Nevertheless, this method is not efficient for modeling the fields in the air gap, as it needs a high number of nodes in order to not sacrifice precision.

1.2. Analytical Methods

Analytical methods have received significant attention because they aid in understanding the physics of the machine and typically require low computational time. Several techniques are used, such as conformal mapping, subdomain, and exact subdomain [5]. These models are based on the Fourier series of the magnetic scalar potential or magnetic vector potential; thus, they are also called Fourier models. An overview of those Fourier-based models and the available techniques is found in [6]. The limit of most Fourier models is that they are based on assumptions, such as idealized geometries and the absence of magnetic saturation. Researchers have made great efforts to consider the saturation of iron parts in Fourier models. In [7,8], global saturation is calculated as the same value as that of permeability in one region. In [9], the permeability distribution in a region is expressed as a Fourier series, so that the permeability can be directly redefined. However, such improvements render the methods very complicated and time-consuming.

1.3. Hybrid Methods

In 1995, a hybrid method [10] was proposed that uses a Fourier model in air gaps and magnets while using finite element analysis in other regions, which is useful in brushless direct-current permanent-magnet (PM) machines. After that, other works combining numerical and analytical methods were published. Y. Laoubi et al. coupled the RN and scalar potential analytical model in a linear permanent-magnet machine in [11]. They also modeled the flux-switching permanent-magnet machine in open-circuit conditions by meshing the stator and rotor into RNs, and connecting them by introducing the harmonics of the scalar potential in the air gap [12]. However, their study only focused on linear machines. L. J. Wu et al. combined the complex permeance method (CPM) with nonlinear RN by transforming magnetic potential distribution in the stator into the equivalent current on the stator bore in the surface-mounted PM machines, and calculated the iron saturation in open-circuit and on-loaded conditions [13,14]. Z. K. Li et al. considered the local saturation of tooth tips on the basis of a combination of CPM and RN [15]. According to [16], the CPM can lead to an error when the slot opening is large, which is a limitation of [13–15]. The methods in [17] use a subdomain to calculate the fields in the slots, so the shape of the slots that can be modeled is limited. H. Yin et al. built an RN model in the stator core and coupled the subdomain model on the stator bore by introducing equivalent current sheets into the slots to solve the nonlinearity effect of the stator for surface-mounted permanent-magnet machines [18]. Y. Zhu et al. combined the subdomain method and an RN to calculate permanent-magnet Vernier machines [19]. The methods in [18,19] used equivalent current sheets to resolve the saturation effect, which does not allow for the calculation of local saturation. B. L. Chikouche et al. built a hybrid model in flat permanent-magnet linear machines, and combined the exact subdomain in the air, slots, and PMs with RN in the teeth and rotor [20]. However, in [20], the calculation is performed for two specific permeabilities of iron and not for actual nonlinear iron. Ouagued et al. combined the analytical method and an RN for calculations in other types of machines, namely, tubular linear machines and flat linear machines [21,22].

1.4. This Article

In this article, a hybrid analytical model based on the scalar potential analytical model and nonlinear RN model is presented for inner-rotor surface-mounted permanent-magnet machines. The rotor and the air gap are modeled with an analytical model, while the stator and slots are modeled with an RN model. The RN can be adapted to different slot types. Different from the subdomain method and other hybrid methods, the method that we propose uses sector-shaped and rectangular elements to deal with the shape of the slots and the shape of straight teeth, respectively. Contrary to [13,17,19], the current in the slots in our study is characterized by an equivalent magnetomotive force (MMF) in the teeth and slots, and the nonlinearity effect of the stator is solved through updating and iterating the permeability of each branch in the RN model.

In [13,17,18], the saturation is modeled only in relatively large areas because there is only one magnetic reluctance in the transverse direction of each tooth. However, the method that we propose allows for the choice of dense or sparse magnetic reluctance, which can take local saturation into account.

The coupling of the two models is direct, and the topology of the network does not change with the motion of the rotor. The whole model has the advantages of the analytical model and of the nonlinear RN model: high calculation speed and accuracy, and taking into consideration of the stator saturation. The whole model uses the symmetry factor to reduce the size of the matrix and speed up the calculation.

The model allows for predicting the magnetic flux density, flux linkage, back EMF, and torque in surface-mounted permanent-magnet machines. The number of elements in the RN can be changed depending on the accuracy needed under saturation conditions. Two types of surface-mounted permanent-magnet machines were modeled to validate the accuracy and speed of this type of model.

The two types of machines were modeled through 18 different HAM simulations and 63 FEM simulations to better understand the relationship between the accuracy and speed of this type of model compared to FEM. In previous articles, we did not find a comparison between hybrid models and FEM, where different levels of precision were calculated for both types of models.

In summary, this article's contributions include the consideration of local saturation and the comparison of different HAM to FEM simulations in terms of the size of the matrix and torque error.

2. Hybrid Model

The geometry and some parameters of the machine are shown in Figure 1. As there is no saturation in the rotor yoke iron, it is assumed to have infinite permeability. The PM and air gap areas are modeled using an analytical model based on the magnetic scalar potential in the cylindrical coordinate system. The permeability of the air between the magnets is assumed to be the same as that of the magnets. The stator is meshed into a reluctance network that is also based on the magnetic scalar potential. As a result, the whole machine is calculated on the basis of a hybrid model that combines the analytical and RN models. The modeled area is divided into three regions (starting from the center): PM (Region I), air gap (Region II), and stator (Region RN). The end effect in the axial direction is neglected. Therefore, the magnetic scalar potential is invariant in the z direction.

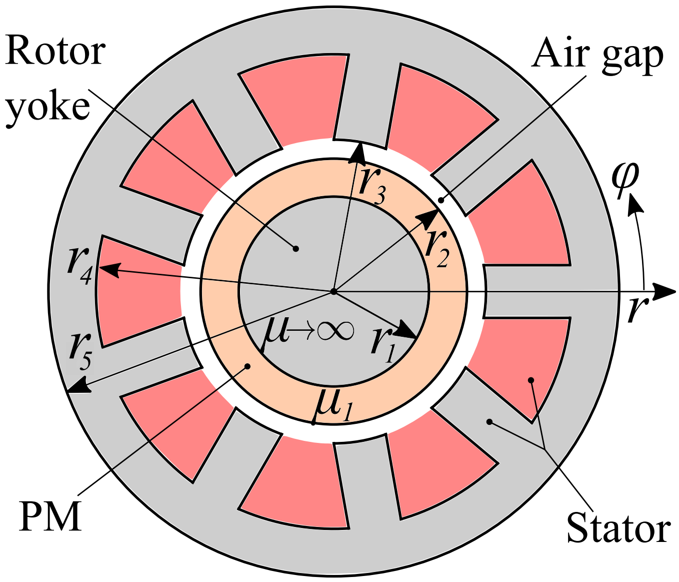

Figure 1. Geometry and parameters of the machine.

2.1. Analytical Model in PMs and Air Gap

The general expressions of the scalar potential distributions in the PM (Region I) and the air gap (Region II) can be expressed as follows [23]:

$$U^{\mathrm{I}} = \sum_k \Big[\Big(A_{1k} r^{qk} + B_{1k} r^{-qk} + P_{\mathrm{C}k}(r) \Big) \cos(qk\varphi) + \Big(C_{1k} r^{qk} + D_{1k} r^{-qk} + P_{\mathrm{S}k}(r) \Big) \sin(qk\varphi) \Big] \tag{1}$$

$$U^{\mathrm{II}} = \sum_k \Big[\Big(A_{2k} r^{qk} + B_{2k} r^{-qk} \Big) \cos(qk\varphi) + \Big(C_{2k} r^{qk} + D_{2k} r^{-qk} \Big) \sin(qk\varphi) \Big], \tag{2}$$

in which

$$P_{\mathrm{C}k}(r) = \begin{cases} \frac{B_{\mathrm{RC}k} r \ln r}{2\mu_1} & qk = 1 \\ \frac{B_{\mathrm{RC}k} r}{\mu_1 (1 - q^2 k^2)} & \text{otherwise} \end{cases} \tag{3}$$

$$P_{\mathrm{S}k}(r) = \begin{cases} \frac{B_{\mathrm{RS}k} r \ln r}{2\mu_1} & qk = 1 \\ \frac{B_{\mathrm{RS}k} r}{\mu_1 (1 - q^2 k^2)} & \text{otherwise,} \end{cases} \tag{4}$$

with

$$B_{\mathrm{R}k} = B_{\mathrm{Rr}k} + qk B_{\mathrm{R}\varphi k} \tag{5}$$

$$B_{\mathrm{RC}k} = B_{\mathrm{R}k} \cos(qk\Omega t + qk\varphi_0) \tag{6}$$

$$B_{\mathrm{RS}k} = B_{\mathrm{R}k} \sin(qk\Omega t + qk\varphi_0), \tag{7}$$

where q is the order of the rotational symmetry of the machine that is equal to the greatest common divisor (GCD) between the number of slots N_s and the number of pole pairs p, assuming that the rotational symmetry also includes the winding. Parameter μ_1 is the permeability of the PMs, Ω is the rotational velocity of the PM area, φ_0 is the PMs' initial position. A_{1k}, B_{1k}, C_{1k}, D_{1k}, A_{2k}, B_{2k}, C_{2k}, and D_{2k} are constants. $B_{\mathrm{Rr}k}$ and $B_{\mathrm{R}\varphi k}$ is the radial and tangential remanent magnetic flux density at the kth harmonic number. For parallel magnetization, we have:

$$B_{\mathrm{R}rk} = \begin{cases} B_{\mathrm{R}}\alpha_{\mathrm{p}}(f_{1k} + f_{2k}) & k/p = 1,3,5\ldots \\ 0 & \text{otherwise} \end{cases} \tag{8}$$

$$B_{\mathrm{R}\varphi k} = \begin{cases} B_{\mathrm{R}}\alpha_{\mathrm{p}}(f_{1k} - f_{2k}) & k/p = 1,3,5\ldots \\ 0 & \text{otherwise} \end{cases} \tag{9}$$

with

$$f_{1k} = \frac{\sin\left((qk+1)\alpha_{\mathrm{p}}\frac{\pi}{2p}\right)}{(qk+1)\alpha_{\mathrm{p}}\frac{\pi}{2p}} \tag{10}$$

$$f_{2k} = \begin{cases} 1 & qk = 1 \\ \frac{\sin\left((qk-1)\alpha_{\mathrm{p}}\frac{\pi}{2p}\right)}{(qk-1)\alpha_{\mathrm{p}}\frac{\pi}{2p}} & \text{else,} \end{cases} \tag{11}$$

where B_{R} is the remanent magnetization of the PM, α_{p} is the PM span ratio, and p is the pole pair number of the machine. The harmonic number k is taken within a finite range for the calculation of the result.

2.2. Reluctance Network Model in Stator

2.2.1. Calculation of Reluctances

The stator part is divided into a mesh-based reluctance network where fluxes flow among different elements through the reluctances. In each element, the radial and circumferential components of fluxes are considered. So, each element that contains four reluctances (two in each direction) is connected by a node at its midpoint. Each element is identified by node number i. Each reluctance of magnetic material has its permeability (μ) and is characterized by a nonlinear $B(H)$ curve. Two typical kinds of mesh elements are illustrated in Figure 2. Elements in a cylindrical layer (Figure 2a) are used in the slots and the stator yoke, where r_i^+ and r_i^- are the outer and inner radii of element i, respectively. Variable r_i^0, which represents the radius of node i, is the average value of r_i^+ and r_i^-. Variables $\Delta\varphi_i^+$, $\Delta\varphi_i^-$, and $\Delta\varphi_i^0$ are the span angles at the corresponding radii. As shown in Appendix B, the reluctance formulas are expressed as follows:

$$R_{i1} = \frac{(r_i^0 - r_i^-)}{\mu l_a (r_i^0\Delta\varphi_i^- - r_i^-\Delta\varphi_i^0)} \ln\left(\frac{r_i^0\Delta\varphi_i^-}{r_i^-\Delta\varphi_i^0}\right) \tag{12}$$

$$R_{i3} = \frac{(r_i^+ - r_i^0)}{\mu l_a (r_i^+\Delta\varphi_i^0 - r_i^0\Delta\varphi_i^+)} \ln\left(\frac{r_i^+\Delta\varphi_i^0}{r_i^0\Delta\varphi_i^+}\right) \tag{13}$$

$$R_{i2} = R_{i4} = \frac{(r_i^+\Delta\varphi_i^- - r_i^-\Delta\varphi_i^+)}{2\mu l_a (r_i^+ - r_i^-)} \frac{1}{\ln\left(\frac{r_i^+\Delta\varphi_i^-}{r_i^-\Delta\varphi_i^+}\right)}. \tag{14}$$

The stator yoke is meshed into sector-shaped elements. Thus, the above span angles are equal $\left(\Delta\varphi_i^+ = \Delta\varphi_i^- = \Delta\varphi_i^0\right)$. Figure 2b shows the rectangular element in the teeth, of which the reluctances depend on the mesh size (w_i and h_i) and are expressed as follows:

$$R_{i1} = R_{i3} = \frac{h_i}{2\mu l_a w_i} \tag{15}$$

$$R_{i2} = R_{i4} = \frac{w_i}{2\mu l_a h_i}. \tag{16}$$

If the tooth's shape is changed into a sector, we can use the reluctance elements of the cylindrical layer. For the slots, we only modify $\Delta\varphi_i^-$ and $\Delta\varphi_i^+$ in (12) to (14).

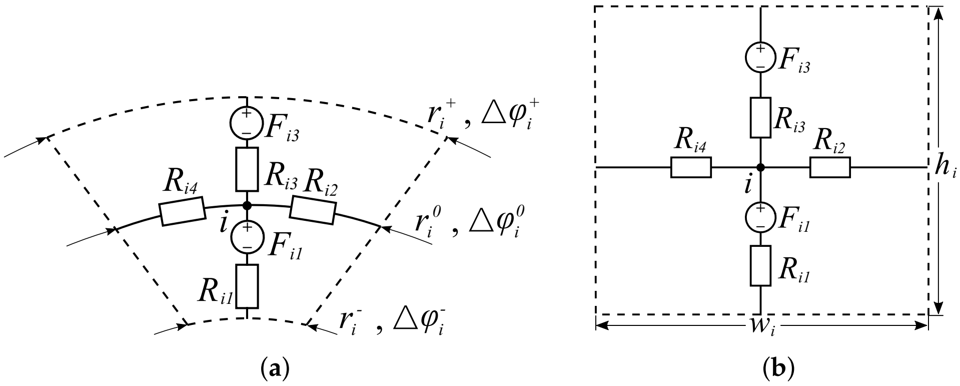

Figure 2. Two typical mesh elements: (**a**) bidirectional reluctances in a cylindrical layer and (**b**) rectangular bidirectional reluctances.

2.2.2. Arrangement of Mesh Elements

A periodical boundary condition is used to decrease the computing time. Only $1/q$ of the stator geometry is modeled into a reluctance network, as we have q symmetric parts. To apply the boundary conditions, the magnetic potential on the two sides is equal, and the fluxes are continuous from one side to another, which means that the two sides are connected. The stator is meshed into different elements. Figure 3 illustrates the arrangement of the elements. The fluxes are assumed to not cross the outer surface of the stator yoke. The fluxes are, hence, along the circumferential direction on the surface, so the radial reluctance connected with the external air is infinitely large.

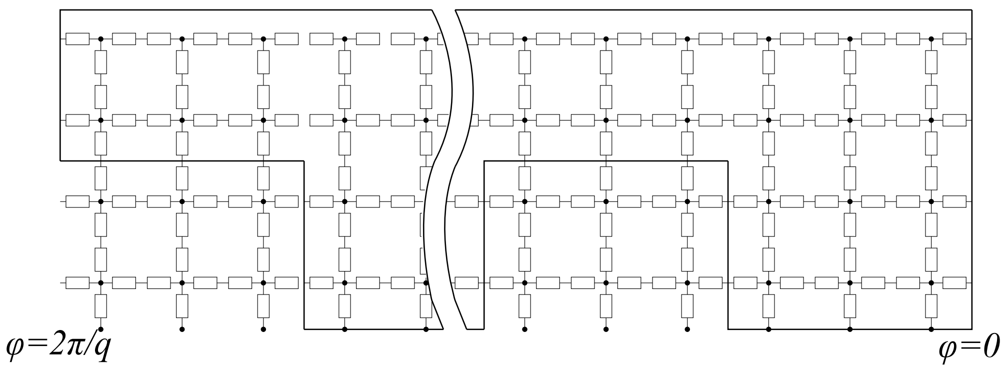

Figure 3. Reluctance network in the stator.

The mesh element numbers in the radial and circumferential directions are n_r and n_c, respectively. The size of the mesh elements is adjustable. Proper size is necessary for good accuracy and reasonable computation time.

Besides the nodes at the midpoint of the mesh element, there are additional n_c nodes on the internal surrounding of the stator that connect the two regions as shown in Figure 3. Hence, the total number of nodes is $n_c n_r + n_c$. The nodes are connected by branches that consist of the reluctance of the adjacent elements. The total number of branches is $2n_c n_r$.

In this article, the nodes are numbered from inner to outer along the counterclockwise direction. As shown in Figure 4, the node and branch numbers are marked in normal and bold lettering, respectively, and the default directions of fluxes are specified.

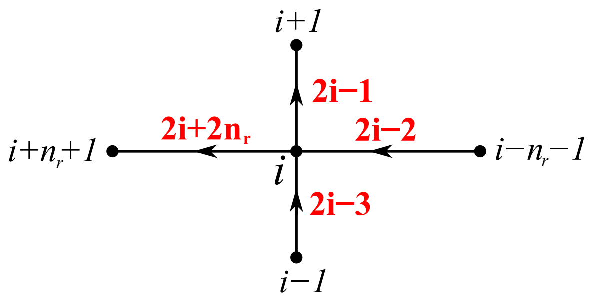

Figure 4. Node- and branch-numbering rule.

2.2.3. Calculation of Magnetic Source

The effects of the armature reaction are represented by magnetic potential sources in certain elements. In this article, the magnetic potential sources are distributed in the teeth and slots elements according to their areas, and only in the radial branches, as shown in Figure 2. They are given by:

$$F_{i1} = F_{i3} = \frac{h_i}{2h} F_{\mathrm{m}t}, \tag{17}$$

where h is the height of the tooth, $F_{\mathrm{m}t}$ is the total MMF of the column where the ith node is located, and F_{i1} and F_{i3} are shown in Figure 2.

In this article, the structures used concentrated winding, so according to Ampère's law, the total MMF for each column in the teeth is:

$$F_{\mathrm{m}t} = N i_t, \tag{18}$$

where i_t is the current in the coil of tth tooth, and N is the number of turns of the whole coil. The total MMF for each column in the slot is only partially generated by the external coil:

$$F_{\mathrm{m}t} = \frac{\Delta\varphi_0 - \Delta\varphi_i}{\Delta\varphi_0} N i_t, \tag{19}$$

where $\Delta\varphi_0$ is the span of a half slot, and $\Delta\varphi_i$ is the span of element i toward the tooth. So, the specific value of $F_{\mathrm{m}t}$ in one tooth and slots beside it is calculated as shown in Figure 5. Then, $F_{\mathrm{m}t}$ in different teeth is obtained in the same way by varying the current.

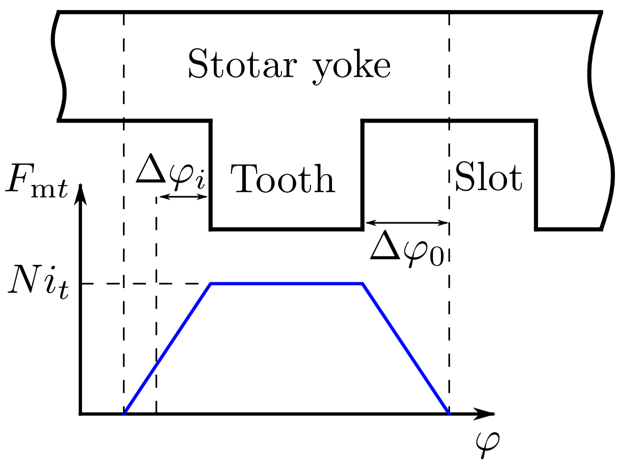

Figure 5. Total magnetic potential sources in the tooth and slots beside it in the radial direction.

2.2.4. Nodal Potential Equation

The magnetic circuit is equivalent to the electric circuit, since both satisfy Kirchhoff's law, so the reluctance network can be solved with the nodal potential equation. The total amount of magnetic flux flowing into and out of any node is zero at any time, and the equation in matrix form is expressed accordingly as follows:

$$\mathbf{A} \cdot \mathbf{\Phi} = \mathbf{0}, \tag{20}$$

where $\mathbf{A}$ with $n_c n_r + n_c$ rows and $2n_c n_r$ columns is the association matrix of branches and nodes. Figure 4 illustrates the ith node; hence, the ith row of matrix $\mathbf{A}$ is expressed as

$$\mathbf{A}_{i,\{2i-3,2i-2,2i-1,2i+2n_r\}} = \{-1,-1,1,1\}. \tag{21}$$

The matrix $\mathbf{\Phi}$ contains the list of branch fluxes. The relationship among the branch permeance, magnetic potential drop, and fluxes is

$$\mathbf{\Phi} = \mathbf{Y} \cdot \mathbf{U_B} \tag{22}$$

with

$$\mathbf{Y} = \begin{bmatrix} \frac{1}{R_1} & & & \\ & \frac{1}{R_2} & & \\ & & \ddots & \\ & & & \frac{1}{R_{2n_c n_r}} \end{bmatrix} \tag{23}$$

where $\mathbf{Y}$ is a diagonal matrix consisting of branch permeances, R_i is the total reluctances of ith branch, and $\mathbf{U_B}$ is the list of branch magnetic potential drops that can be expressed as follows:

$$\mathbf{U_B} = \mathbf{A}^T \cdot \mathbf{U_N} + \mathbf{U_S}, \tag{24}$$

where $\mathbf{U_S}$ is the list of branch magnetic sources, $\mathbf{U_N}$ is the list of node magnetic potential. The nodal potential equation can be deduced as follows:

$$\mathbf{A} \cdot \mathbf{Y} \cdot \mathbf{A}^T \cdot \mathbf{U_N} + \mathbf{A} \cdot \mathbf{Y} \cdot \mathbf{U_S} = \mathbf{0}. \tag{25}$$

2.3. Coupling of the Two Models

In this section, we explain how the RN model in the stator is connected with the analytical scalar potential distribution in the air gap.

2.3.1. Harmonic Form of Nodal Magnetic Potential

The nodal magnetic potential in the RN model is discrete values. Thus, the magnetic potential on the boundary is a sequence of discrete data. The number of data equals the number of nodes on the boundary. Instead of interpolation, the step function shown in Figure 6 is used.

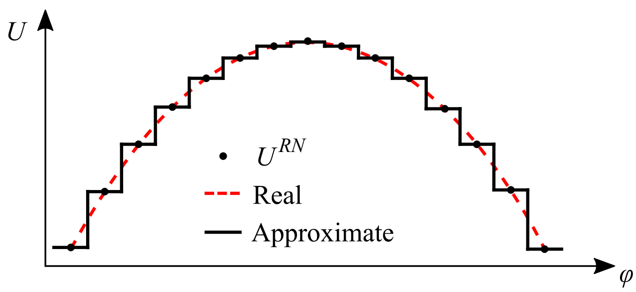

Figure 6. Approximate function of magnetic potential on the boundary.

We take the Fourier series of U^{RN}:

$$U^{\mathrm{RN}}|_{r=r_3} = \sum_k \left[C_k^{\mathrm{FS}} \cos(qk\varphi) + S_k^{\mathrm{FS}} \sin(qk\varphi) \right]. \tag{26}$$

with C_k^{FS} and S_k^{FS}, the kth coefficients of FS, and is calculated as follows:

$$C_k^{\mathrm{FS}} = \frac{q}{\pi} \sum_{i=1}^{n_c} \int_{\varphi_{i1}}^{\varphi_{i2}} U_i^{\mathrm{RN}} \cos(qk\varphi) d\varphi \tag{27}$$

$$S_k^{\mathrm{FS}} = \frac{q}{\pi} \sum_{i=1}^{n_c} \int_{\varphi_{i1}}^{\varphi_{i2}} U_i^{\mathrm{RN}} \sin(qk\varphi) d\varphi, \tag{28}$$

where φ_{i1} and φ_{i2} are the two angle positions where element i is located, as shown in Figure 7. Variable k is finite in the calculation, and its maximal value is the same as that in the analytical model. According to Nyquist–Shannon's theorem, the number of nodes should not be less than twice the total harmonic number in order to avoid errors in the calculation of the flux density at the middle of the air gap of machines.

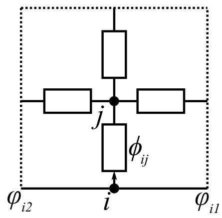

Figure 7. The element on the boundary.

2.3.2. Boundary Conditions at r_3

The two boundary conditions at r_3 are:

$$\left(\overrightarrow{B}^{\mathrm{FS}} |_{r=r_3} - \overrightarrow{B}^{\mathrm{II}} |_{r=r_3} \right) \cdot \overrightarrow{n} = 0 \tag{29}$$

$$\left(\overrightarrow{H}^{\mathrm{FS}} |_{r=r_3} - \overrightarrow{H}^{\mathrm{II}} |_{r=r_3} \right) \cdot \overrightarrow{t} = 0. \tag{30}$$

The first boundary condition, (29), implies that the fluxes through the boundary are continuous. On node i,

$$P_{ij}(U_i - U_j) = -\mu_0 l_a r_3 \int_{\varphi_{i1}}^{\varphi_{i2}} \frac{\partial U^{\mathrm{II}}}{\partial r} |_{r=r_3} d\varphi. \tag{31}$$

The final expression is

$$\begin{aligned} P_{ij}(U_i - U_j) + \mu_0 l_a r_3 \sum_k A_{2k} qk r_3^{qk-1} \int_{\varphi_{i1}}^{\varphi_{i2}} \cos(qk\varphi) d\varphi \\ + \mu_0 l_a r_3 \sum_k B_{2k}(-qk) r_3^{-qk-1} \int_{\varphi_{i1}}^{\varphi_{i2}} \cos(qk\varphi) d\varphi \\ + \mu_0 l_a r_3 \sum_k C_{2k} qk r_3^{qk-1} \int_{\varphi_{i1}}^{\varphi_{i2}} \sin(qk\varphi) d\varphi \\ + \mu_0 l_a r_3 \sum_k D_{2k}(-qk) r_3^{-qk-1} \int_{\varphi_{i1}}^{\varphi_{i2}} \sin(qk\varphi) d\varphi = 0. \end{aligned} \tag{32}$$

From the second boundary condition, (30), the following expression is obtained:

$$\frac{\partial U^{\mathrm{RN}}}{\partial \varphi}\,|_{r=r_3}=\frac{\partial U^{\mathrm{II}}}{\partial \varphi}\,|_{r=r_3}\,, \tag{33}$$

which means that, for each harmonic k,

$$C_k^{\mathrm{FS}} = A_{2k}r_3^{qk} + B_{2k}r_3^{-qk} \tag{34}$$

$$S_k^{\mathrm{FS}} = C_{2k}r_3^{qk} + D_{2k}r_3^{-qk}. \tag{35}$$

Lastly, the following expressions are derived:

$$A_{2k}r_3^{qk} + B_{2k}r_3^{-qk} = \sum_{i=1}^{n_c} U_i^{\mathrm{RN}} \frac{q}{\pi} \int_{\varphi_{i1}}^{\varphi_{i2}} \cos(qk\varphi)d\varphi \tag{36}$$

$$C_{2k}r_3^{qk} + D_{2k}r_3^{-qk} = \sum_{i=1}^{n_c} U_i^{\mathrm{RN}} \frac{q}{\pi} \int_{\varphi_{i1}}^{\varphi_{i2}} \sin(qk\varphi)d\varphi. \tag{37}$$

2.4. Matrix Form

In the analytical model, n_{H} is the total considered harmonic number. For each harmonic in each area, four constants need to be calculated. In the PM and the air gap, $4 \times n_{\mathrm{H}} \times 2 = 8n_{\mathrm{H}}$ constants are unknown in total.

In the RN model, the machine is meshed into n_c elements in the circumferential direction and n_r elements in the radial direction. Each element has a node. There are additional n_c nodes on the boundary. The potential of each node needs to be calculated. Thus, $n_c n_r + n_c$ constants are unknown. We have $n_c \geq 2n_{\mathrm{H}}$.

Therefore, the total number of unknowns is $8n_{\mathrm{H}} + n_c n_r + n_c$. In the analytical model, the boundary conditions on r_1 and r_2 give $2n_{\mathrm{H}}$ and $4n_{\mathrm{H}}$ equations, respectively. In the RN model, Kirchhoff's law gives $n_c n_r$ equations. (36), (37) and (32) give n_{H}, n_{H}, n_c equations, respectively. Then, a set of $8n_{\mathrm{H}} + n_c n_r + n_c$ dimensional equations are established. Equation (38) shows the matrix form of the equations. The expression of the matrices is given in Appendix A.

$$\left[\begin{array}{cc|c} \multicolumn{2}{c|}{\multirow{2}{*}{\mathbf{G}}} & \mathbf{0} \\ \cline{3-3} & & \mathbf{M} \\ \hline \mathbf{0} & \multicolumn{1}{|c|}{\mathbf{Q}} & \mathbf{A}\cdot\mathbf{Y}\cdot\mathbf{A}^T \end{array}\right] \cdot \left[\begin{array}{c} \mathbf{K} \\ \hline \mathbf{U_N} \end{array}\right] = \left[\begin{array}{c} -\mathbf{T} \\ \hline -\mathbf{A}\cdot\mathbf{Y}\cdot\mathbf{U_S} \end{array}\right] \tag{38}$$

2.5. Nonlinear Analysis

Considering the magnetic nonlinearity of the stator material, the permeability of the iron part is related to the magnetic field. The branch magnetic field strength can be calculated as follows:

$$H = \frac{U_B}{\triangle l}, \tag{39}$$

where U_B is the potential drop in a branch, and $\triangle l$ the equivalent length of the branch path. According to the obtained magnetic strength in each step, an interpolation is performed on the magnetization curve of the lamination material to obtain the relative permeabilities of all the nonlinear branches, which are used to update the matrix equation until it is convergent. This procedure to deal with the nonlinear system is illustrated as a flowchart in Figure 8. At the beginning of the program, the relative permeabilities are initialized as μ^0. For step m (m = 1, 2,..., N_0, with N_0 being the maximal iteration steps given), $\mathbf{Y}^{m-1}$ is calculated, and Equation (38) is solved. The permeabilities are then updated as $\mu^m = \mu(\mathbf{H}^{m-1})$. The iteration finishes once it converges to $\|\mu^m - \mu^{m-1}\| < \epsilon$, with ϵ being the given accuracy.

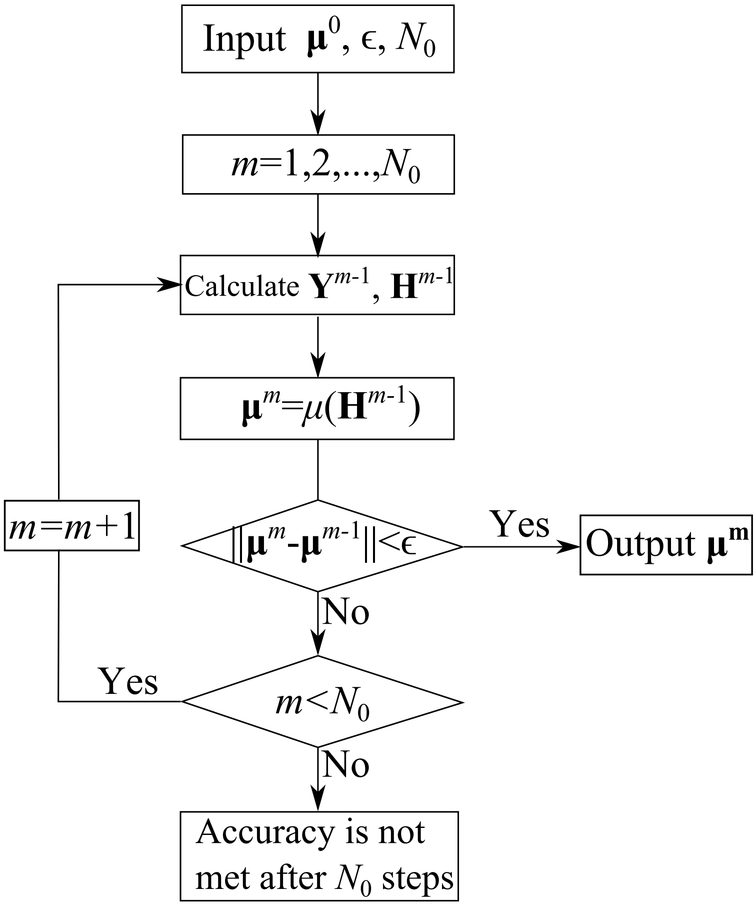

Figure 8. Iteration process.

2.6. Post-Processing

Once the nonlinear system is solved, the magnetic potential on each node on the stator side, and the harmonics of magnetic potential in the air gap and PMs are obtained. Then, the back EMF and torque of the machine can be derived through postprocessing. In RN regions, the magnetic strength is calculated using Equation (39). In the air gap and PM regions, it can be expressed as the derivatives of magnetic potential [24]:

$$H_r = -\frac{\partial U}{\partial r}, \tag{40}$$

$$H_\varphi = -\frac{1}{r}\frac{\partial U}{\partial \varphi}. \tag{41}$$

Once the magnetic field is obtained, the flux linkage in each coil can be calculated from

$$\Psi_i(t) = \mu_0 r_3 l_a N \int_{\beta_i-\tau/2}^{\beta_i+\tau/2} \kappa \xi_i H_r(r_3, \varphi, t) d\varphi, \tag{42}$$

where N is the number of turns of each coil ($\kappa = 1$ or -1 depending on the direction of winding), ξ_i is the coefficient that approximates the flux leakage in the slots where the coil conductors are placed and are expressed as a function of φ,

$$\xi_i = \begin{cases} 1 & \text{if } |\varphi - \beta_i| \le \frac{\delta}{2} \\ \frac{\tau - 2|\varphi - \beta_i|}{\tau - \delta} & \text{if } \frac{\delta}{2} \le |\varphi - \beta_i| \le \frac{\tau}{2}, \end{cases} \tag{43}$$

where β_i is the angle of the axis of coil i, and δ and τ are the span angles of the innermost and outermost conductors of a coil, respectively, as shown in Figure 9.

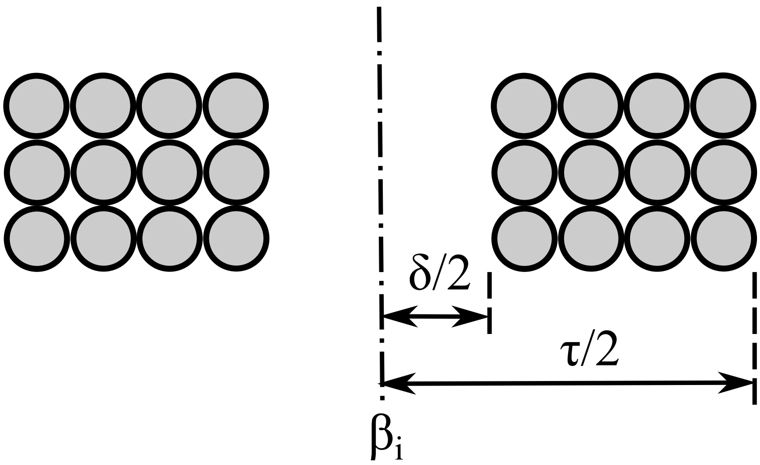

Figure 9. Sectional view of coil i.

The phase flux linkage can be calculated by summing up all the coil flux linkages in each phase:

$$\Psi_{\text{ph}}(t) = \sum_{\text{coil } i \in \text{ph}} \Psi_i(t), \text{ with ph} = A, B, \text{and } C. \tag{44}$$

Instead of predicting the flux leakage via an approximative coefficient, the authors in [13] provided a method that obtained the flux leakage from the RN side. After obtaining the flux linkages at different rotor positions by rotating a small step in Δt time, which can be regarded as a time-varying function, the back EMF can be deduced with

$$E_{\text{ph}} = \frac{\Delta \Psi_{\text{ph}}}{\Delta t} \tag{45}$$

where $\Delta \Psi_{\text{ph}}$ is the difference of the flux linkage of any phase in one step.

By integrating the Maxwell stress tensor along a circle in the air gap, the instantaneous electromagnetic torque can be calculated using the radial and circumferential components of flux strength. Torque

$$T = \mu_0 l_a r^2 \int_0^{2\pi} H_r H_\varphi d\varphi, \tag{46}$$

can be expended as follows:

$$\begin{aligned} T &= \mu_0 l_a r q^2 \pi \\ &\sum_k k^2 \Big[\Big(A_{2k} r^{qk-1} - B_{2k} r^{-qk-1} \Big) \Big(C_{2k} r^{qk} + D_{2k} r^{-qk} \Big) - \\ &\Big(A_{2k} r^{qk} + B_{2k} r^{-qk} \Big) \Big(C_{2k} r^{qk-1} - D_{2k} r^{-qk-1} \Big) \Big], \end{aligned} \tag{47}$$

where r is any radial value in the air gap.

3. Validation

Two surface-mounted permanent-magnet machines were selected as examples for modeling calculation. To illustrate the advantage of the hybrid analytical method in dealing with the nonlinear problem of ferromagnetic materials, the saturation of the stator of the two machines is different: one is not highly saturated, and the other is highly saturated.

The main design specification of the machines is summarized in Table 1, the geometric dimensions are illustrated in Figure 10, and the B–H curves for lamination material are shown in Figure 11. As we wanted to verify the correctness in high-saturation conditions, the teeth of Machine II were designed to be very narrow.

Table 1. Main design specification of the machines.

Parameter	Machine I	Machine II	Unit
Pole pair number	16	3	-
Slot number	36	9	-
Number of turns	113	50	-
Lamination length	140	54	mm
Outer stator radius	180	41	mm
Inner stator radius	134.2	22.3	mm
Outer rotor radius	133.1	21.8	mm
Inner rotor radius	114.5	-	mm
Stator yoke thickness	22	3	mm
Stator tooth width	10.7	3	mm
PM thickness	6.4	2.5	mm
PM span angle	9.2	50	deg
Lamination material	50W470	50W800	-
PM remanent magnetic density	1.32	1.20	T
Permeability of PM	1.31×10^{-6}	1.42×10^{-6}	H/m

The topology and winding distribution of Machines I and II are shown in Figure 12a,b, respectively. An example of RN for the two machines is given in Figure 13. A precise 2D FEM simulation was used to validate the proposed method. More details are in the next section. Meanwhile, the two machines were modeled with the subdomain method, so the comparison between the results shows the characteristics of different methods.

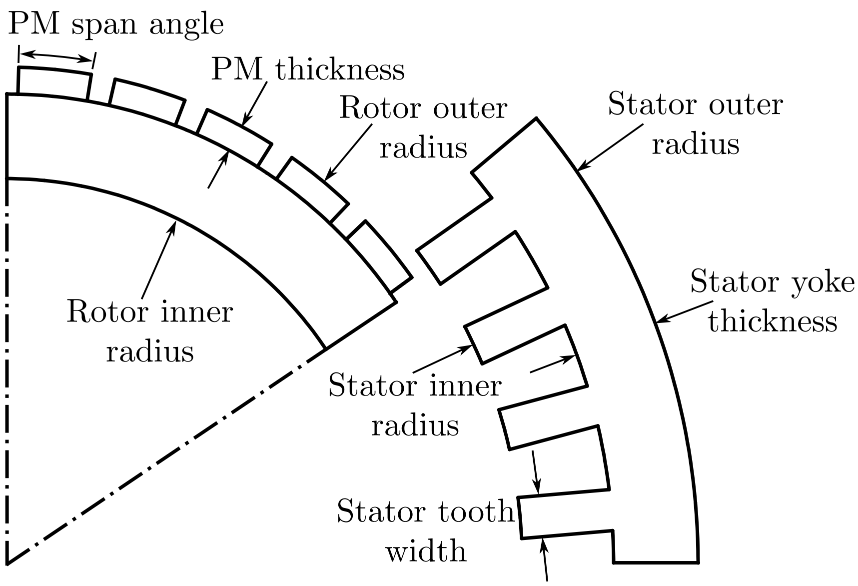

Figure 10. Design parameters of the machines.

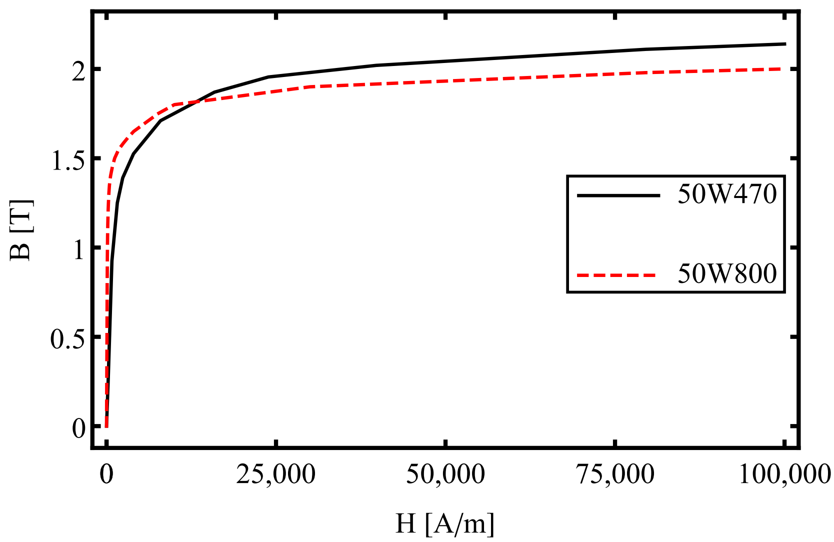

Figure 11. B–H curves for the lamination materials used in Machines I and II.

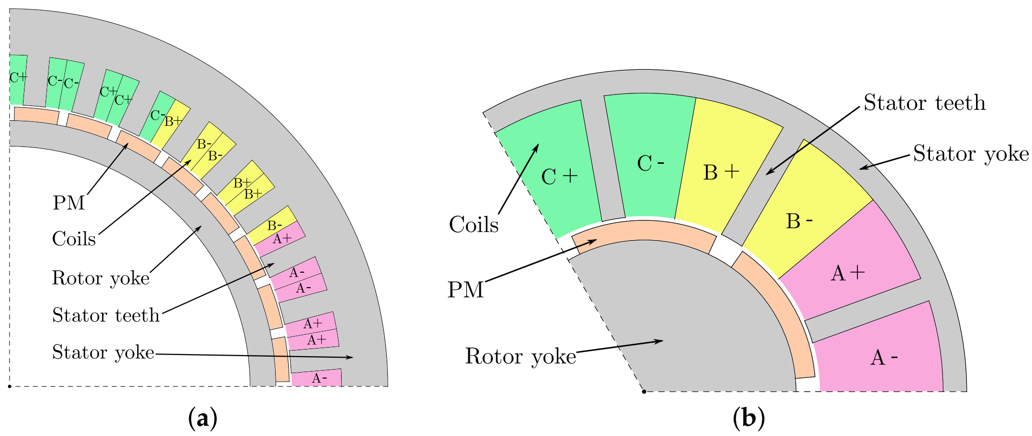

Figure 12. Machine topology: (**a**) Machine I. (**b**) Machine II.

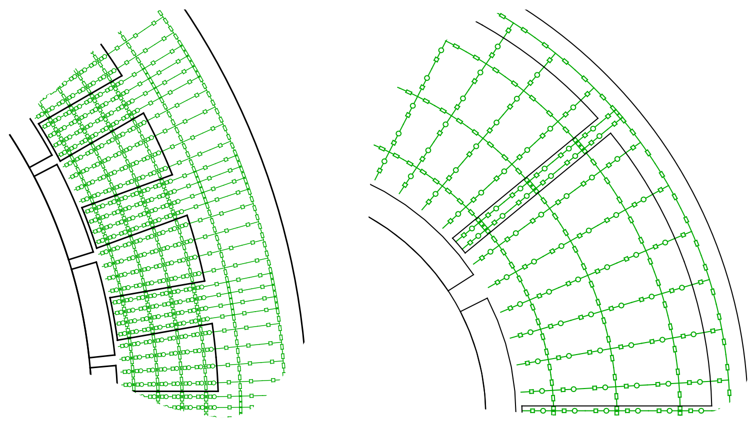

Figure 13. Example of reluctance network for (**left**) Machine I and (**right**) Machine II.

3.1. Fields

The magnetic flux density distributions of both machines were obtained with the HAM, FEM, and subdomain method. The calculation process for the subdomain method was presented in [5]. Open-circuit and loaded condition validations were performed.

Figures 14–17 show a comparison of the magnetic flux density distribution at the middle of the air gap in each machine among the HAM, FEM, and subdomain method.

Phase currents were 0.34, −0.98, and 0.64 A in Machine I, and 0, −6.12, and 6.12 A in Machine II, respectively. The curves show a great agreement between the HAM and the FEM for the radial and circumferential components of magnetic flux density. The difference between the HAM and the subdomain method in Machine I is small because of the low saturation.

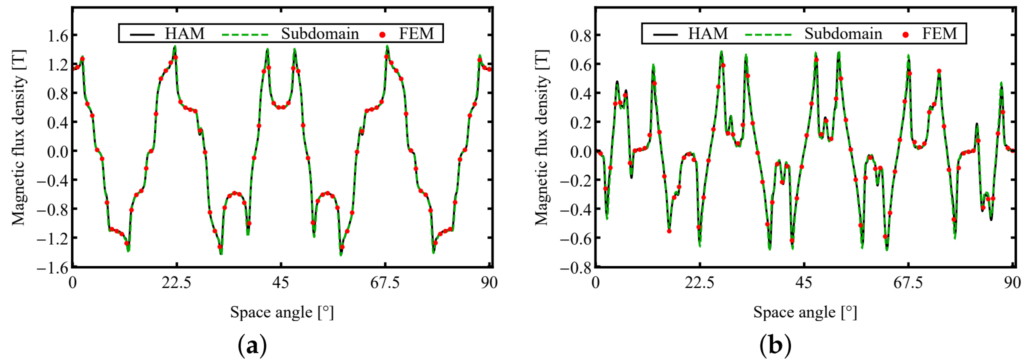

Figure 14. Comparison of the flux density at the middle of the air gap of Machine I in open-circuit condition: (**a**) radial component; (**b**) circumferential component.

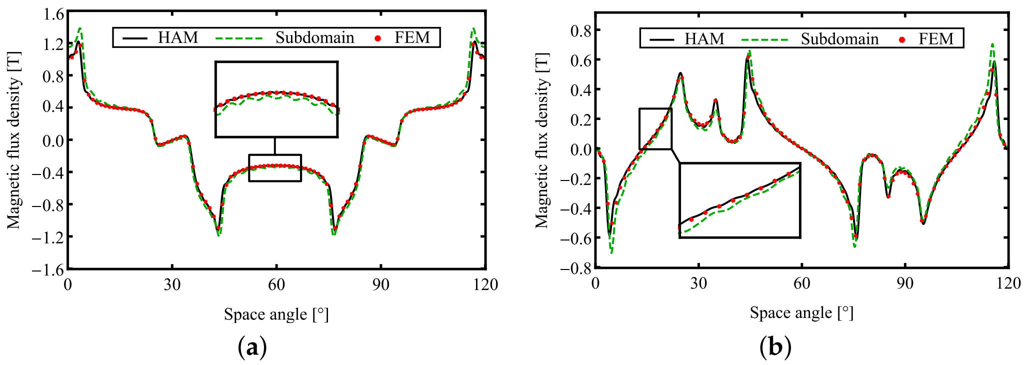

Figure 15. Comparison of the flux density at the middle of the air gap of Machine II in open-circuit condition: (**a**) radial component; (**b**) circumferential component.

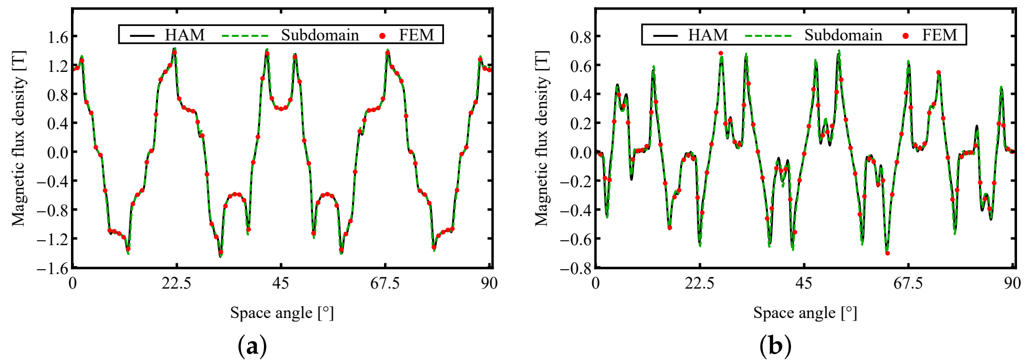

Figure 16. Comparison of the flux density at the middle of the air gap of Machine I with a current of 1 A (maximal amplitude): (**a**) radial component; (**b**) circumferential component.

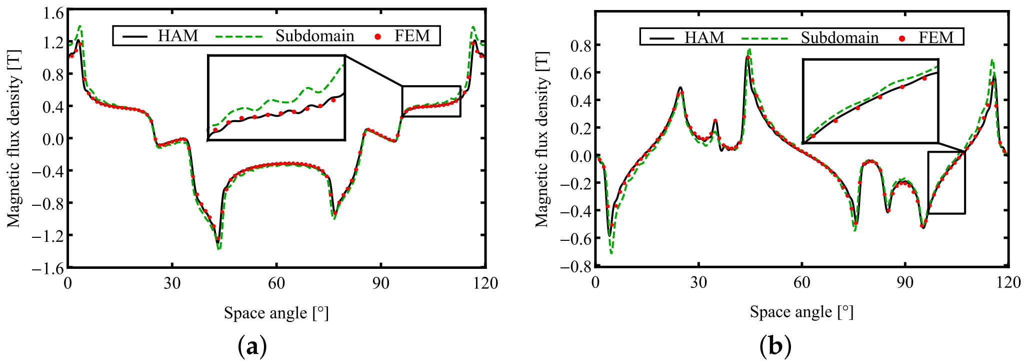

Figure 17. Comparison of the flux density at the middle of the air gap of Machine II with a current of 7 A (maximal amplitude): (**a**) radial component; (**b**) circumferential component.

In Machine II, the results calculated with the subdomain model differ from those calculated by HAM and FEM due to the high saturation.

The highly coincidental results between HAM and FEM show that the HAM is valid in both open-circuit and loaded conditions, even when the material in the machine is saturated.

The mesh parameters in HAM were chosen to be $n_{\mathrm{H}} = 90$, $n_c = 180$, $n_r = 12$ in Machine I, and $n_{\mathrm{H}} = 45$, $n_c = 90$, $n_r = 11$ in Machine II, resulting in matrix sizes of 3060×3060 and 1440×1440, respectively, to be solved. In the FEM, the sizes of the matrices were $16{,}626 \times 16{,}626$ and 8929×8929 including the rotor and air gap parts. To guarantee a fair comparison, the FEM of these two machines use the same symmetry. In the HAM above, the amount of computation was reduced by 70% compared with FEM while keeping the error below 1% in the results of torque.

3.2. Flux and Back EMF

The magnetic fluxes of the two machines were also calculated with the three methods and are presented in Figure 18a,b. Compared with the FEM, the average errors of the flux results of the HAM and the subdomain method were 0.32% and 4.90% in Machine I, and 1.10% and 22.57% in Machine II, respectively.

The back-EMF results of the two machines are presented in Figure 19a,b. Compared with the FEM, the average errors of the HAM and the subdomain method were 0.22% and 5.02% in Machine I, and 3.32% and 23.64% in Machine II, which were similar to the flux results. As the HAM has high accuracy in calculating the magnetic field, the prediction of the magnetic fluxes and back EMF thereby also shows excellent accuracy, while the subdomain method has obvious differences.

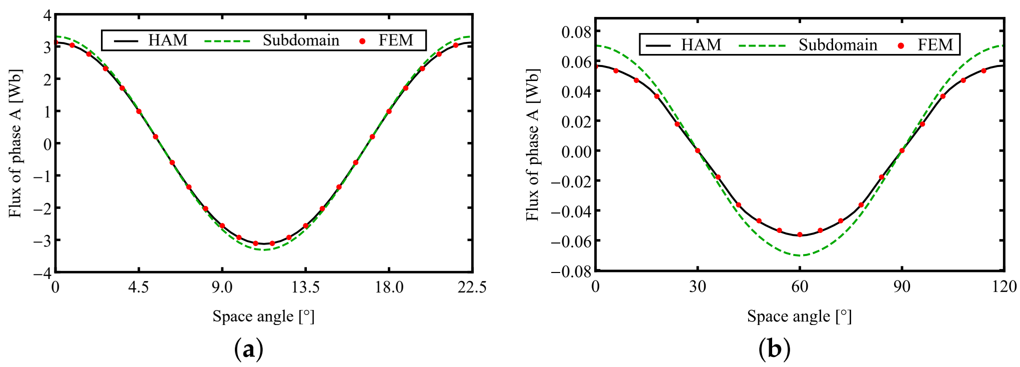

Figure 18. The magnetic flux of Phase A under open-circuit condition: (**a**) Machine I and (**b**) Machine II.

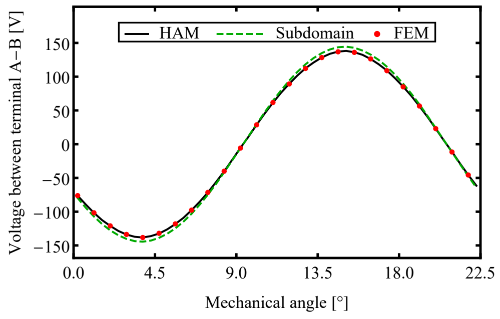

Figure 19. Comparison of back-EMF waveforms between Terminals A and B: (**a**) Machine I and (**b**) Machine II.

3.3. Torque

The relationship between the maximal output torque and the applied direct current is shown in Figure 20a,b. The curve shows that the calculated value of the torque from the HAM was very consistent with the FEM, and the subdomain method was higher. As the iron in the stator of Machine I did not reach high saturation, the torque–current curve is a relatively straight line. Compared with the FEM, the average errors of the torque results of the HAM and the subdomain method were 0.32% and 5.97% in Machine I, and 0.49% and 19.84% in Machine II, respectively.

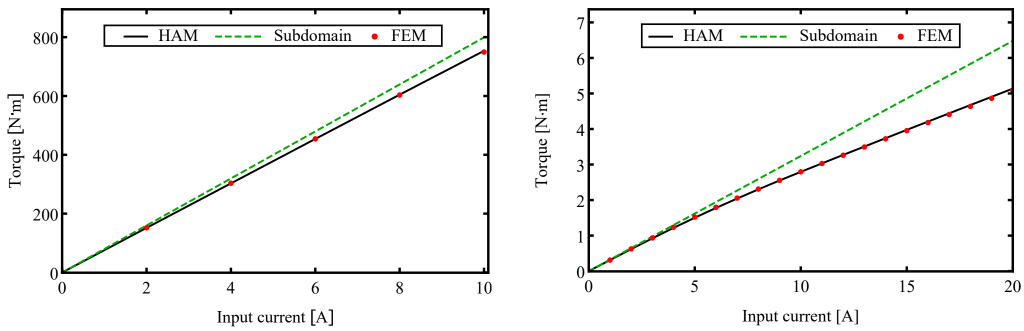

Figure 20. Comparison of electromagnetic torque as a function of the maximal current in the winding: (**a**) Machine I and (**b**) Machine II.

The torque pulsation and cogging torque of the two machines calculated with three methods are presented in Figures 21 and 22. The following errors were calculated using the FEM as a reference. For Machine I with a current of 4 A (maximal amplitude), the average errors given by the HAM and by the subdomain method were 0.27% and 5.41%, respectively. For Machine II with a current of 20 A (maximal amplitude), the average errors of the HAM and the subdomain method were 1.54% and 48.2%, respectively. Therefore, the HAM works well for torque pulsation calculation. In the case of the cogging torque, there is no current; hence, there is minimal saturation. Although in the case with little saturation the benefit of HAM was less obvious, we can still see that for Machines I and II, HAM gave better results than those of the subdomain. There were some errors between HAM and FEM in the cogging torque results of Machine I. The reason is that, contrary to Machine II where the whole tooth saturated, the location of magnetic saturation in Machine I was mainly at the stator tooth tip corners. For the calculation in Figure 21b, the mesh of HAM was denser than the mesh used for the other calculations, as described in Section 3.1. A further increase in mesh density would further diminish the error shown in Figure 21b.

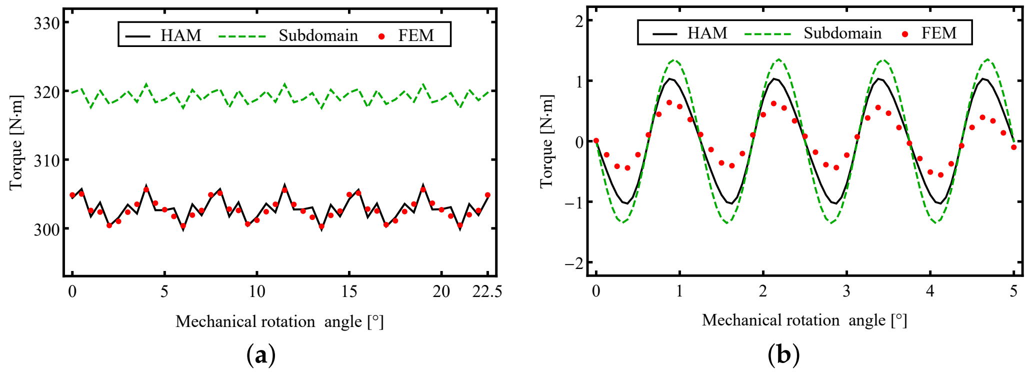

Figure 21. Comparison of torque pulsation of Machine I: (**a**) torque ripple with a current of 4 A (maximal amplitude); (**b**) cogging torque.

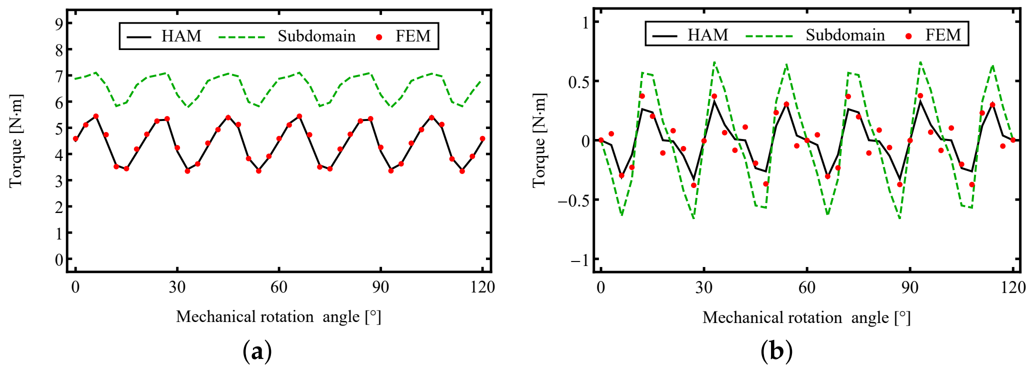

Figure 22. Comparison of torque pulsation of Machine II: (**a**) torque ripple with a current of 20 A (maximal amplitude); (**b**) cogging torque.

Because the magnetic saturation in Machine I was not very high, the differences among HAM, FEM, and the subdomain method were small. The differences in the field results (Figures 14 and 16) are not important. Nevertheless, we can see a slight difference in the flux linkage (Figure 18a), back-EMF (Figure 19a), and torque (Figure 20a) results. As the current increased, the HAM gave results that were more accurate compared to those of the subdomain method. The difference was more significant for Machine II, as its magnetic saturation was higher than that of Machine I.

3.4. Multiple FEM and HAM Simulations

To verify the accuracy of the HAM, the RN of Machines I and II were created with different densities of elements. The calculated torque was compared with that of a high-precision FEM. Meanwhile, the torque results of FEMs modeled with different mesh precision for Machines I and II were compared with the high-precision FEM results. The sizes of the matrix in the high precision FEM of Machines I and II were 31,140 × 31,140 and 26,463 × 26,463, respectively. The main changes in the different FEMs were the mesh size of the air gap and the PMs, taking a low mesh density for the rest of the machine, as those parts affect the precision less.

Figure 23a,b show that, as the number of divisions of RN increased, the matrix size increased, and the HAM calculation results became increasingly accurate. In Figure 23a, some points of the FEM results are on the left-hand side of the HAM results trend line, which means that the HAM for Machine I did not have a clear advantage. However, for Machine II (Figure 23b), all points of the FEM results are on the right-handd side of the HAM results trend line, which means the HAM is valuable and offers a good advantage. The average torque error of 15 FEM simulations with a matrix size of around 1700 × 1700 was 2.62%, and HAM could reduce the error to 0.17% at the same matrix size. The reason for the different results presented by Machines I and II is that Machine I has 9 slots in a symmetrical part, while Machine II only has 3 slots in a symmetrical part. This renders the matrix of Machine I larger than that of Machine II in the HAM calculation, but the minimal number of nodes in the FEM was similar in the two machines. In addition, Figure 23a also shows random errors in the calculation of the FEM, while the HAM had good stability.

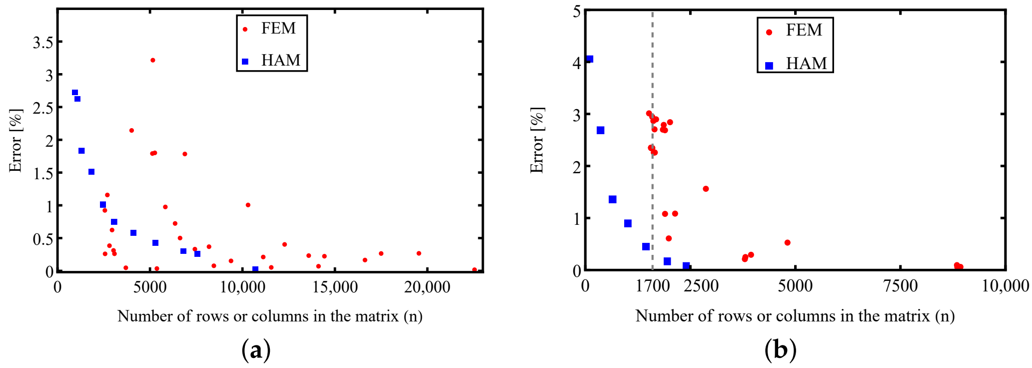

Figure 23. Torque error for different divisions in the HAM and FEM as a function of the sizes of the matrix (n × n): (**a**) Machine I with a current of 4 A (maximal amplitude). (**b**) Machine II with a current of 10 A (maximal amplitude).

In Machine I, the HAM could reduce the torque error from 5.27% in the subdomain method to 0.03% in the HAM with the densest division. In the same way, the HAM could reduce the torque error from 16.8% to 0.08% for Machine II. This verifies that the two machines had different saturation levels, and HAM had a clear advantage over the subdomain method.

4. Conclusions

In this article, an effective and accurate hybrid analytical model that couples a scalar potential analytical model with RN was used to calculate and analyze surface-mounted permanent-magnet machines. The modeling was divided into two parts according to whether saturation exists—the magnets and air gap regions were modeled with an analytical model, while the stator region was modeled with an RN model. Many aspects were taken into account in this model: circuit armature reaction, slotting effect, and especially magnetic saturation. The HAM results for the magnetic flux density, flux linkage, back EMF, torque, and error were compared with those of the FEM and the subdomain method. The size of the matrix could be adjusted according to the number of elements of the RN, depending on the needed accuracy, and different HAM and FEM simulations were compared in terms of the size of the matrix and torque error. Compared with the subdomain method, the calculation results of the HAM show excellent accuracy, and the advantages of the HAM are that saturation in the stator is considered and there is no restriction on the slot type. The HAM can reduce torque error and has great advantages over the subdomain method. Compared with the FEM, the HAM can reduce the size of the matrix that needs to be calculated, which means that the calculation time can be reduced significantly. For a machine with a high number of slots in its symmetrical part, this method has advantages compared to the subdomain method, but not compared to the FEM in its present form, although further optimization of the RN may bring advantages in the HAM. Although in this article the slot per pole per phase is fractional for Machines I and II both, the model can also be applied to machines with an integer ratio. The application of the method can also be extended to other types of machine structures, such as semiopen slot structures and surface-inset permanent-magnet structures. Furthermore, a three-dimensional hybrid analytical model can be built to consider the axial inhomogeneity of the machine.

Author Contributions: Conceptualization W.L., J.Z., Y.F. and P.-D.P.; funding acquisition, W.L., Y.F. and P.-D.P.; investigation, W.L., J.Z. and P.-D.P.; methodology J.Z., W.L. and P.-D.P.; supervision Y.F. and P.-D.P.; Writing—original draft W.L. and J.Z.; Writing—review & editing W.L., J.Z., Y.F. and P.-D.P. All authors have read and agreed to the published version of the manuscript.

Funding: This work was funded by the National Natural Science Foundation of China under grants 52150610491, 51837010, and 51827810.

Data Availability Statement: Not applicable.

Conflicts of Interest: The authors declare no conflict of interest.

Abbreviations

The following abbreviations are used in this manuscript:

HAM	Hybrid analytical model
RN	Reluctance network
PM	Permanent magnet
EMF	Electromotive force
FEM	Finite-element method
CPM	Complex permeance method
MMF	Magnetomotive force

Appendix A

Composition of matrices in Equation (38):

$$\mathbf{G} = \begin{bmatrix} \mathbf{G}_{11} & \mathbf{G}_{12} & & & & & & \\ & & \mathbf{G}_{23} & \mathbf{G}_{24} & & & & \\ \mathbf{G}_{31} & \mathbf{G}_{32} & & & \mathbf{G}_{35} & \mathbf{G}_{36} & & \\ & & \mathbf{G}_{43} & \mathbf{G}_{44} & & & \mathbf{G}_{47} & \mathbf{G}_{48} \\ \mathbf{G}_{51} & \mathbf{G}_{52} & & & \mathbf{G}_{55} & \mathbf{G}_{56} & & \\ & & \mathbf{G}_{63} & \mathbf{G}_{64} & & & \mathbf{G}_{67} & \mathbf{G}_{68} \\ & & & & \mathbf{G}_{75} & \mathbf{G}_{76} & & \\ & & & & & & \mathbf{G}_{87} & \mathbf{G}_{88} \end{bmatrix}$$

$$\mathbf{G}_{11} = \mathbf{G}_{23} = \mathbf{diag}\left\{r_1^{q}, \cdots, r_1^{qk}, \cdots, r_1^{qn_\mathrm{H}}\right\}$$

$$\mathbf{G}_{12} = \mathbf{G}_{24} = \mathbf{diag}\left\{r_1^{-q}, \cdots, r_1^{-qk}, \cdots, r_1^{-qn_\mathrm{H}}\right\}$$

$$\mathbf{G}_{31} = \mathbf{G}_{43} = -\mathbf{G}_{35} = -\mathbf{G}_{47} = \mathbf{diag}\left\{r_2^{q}, \cdots, r_2^{qk}, \cdots, r_2^{qn_\mathrm{H}}\right\}$$

$$\mathbf{G}_{32} = \mathbf{G}_{44} = -\mathbf{G}_{36} = -\mathbf{G}_{48} = \mathbf{diag}\left\{r_2^{-q}, \cdots, r_2^{-qk}, \cdots, r_2^{-qn_\mathrm{H}}\right\}$$

$$\mathbf{G}_{51} = \mathbf{G}_{63} = \frac{\mu_1}{\mu_0} q \cdot \mathbf{diag}\left\{r_2^{q-1}, \cdots, kr_2^{qk-1}, \cdots, n_\mathrm{H} r_2^{qn_\mathrm{H}-1}\right\}$$

$$\mathbf{G}_{52} = \mathbf{G}_{64} = -\frac{\mu_1}{\mu_0} q \cdot \mathbf{diag}\left\{r_2^{-q-1}, \cdots, kr_2^{-qk-1}, \cdots, n_\mathrm{H} r_2^{-qn_\mathrm{H}-1}\right\}$$

$$\mathbf{G}_{55} = \mathbf{G}_{67} = -q \cdot \mathbf{diag}\left\{r_2^{q-1}, \cdots, kr_2^{qk-1}, \cdots, n_\mathrm{H} r_2^{qn_\mathrm{H}-1}\right\}$$

$$\mathbf{G}_{56} = \mathbf{G}_{68} = q \cdot \mathbf{diag}\left\{r_2^{-q-1}, \cdots, kr_2^{-qk-1}, \cdots, n_\mathrm{H} r_2^{-qn_\mathrm{H}-1}\right\}$$

$$\mathbf{G}_{75} = \mathbf{G}_{87} = \mathbf{diag}\left\{r_3^{q}, \cdots, r_3^{qk}, \cdots, r_3^{qn_\mathrm{H}}\right\}$$

$$\mathbf{G}_{76} = \mathbf{G}_{88} = \mathbf{diag}\left\{r_3^{-q}, \cdots, r_3^{-qk}, \cdots, r_3^{-qn_\mathrm{H}}\right\}$$

$$\mathbf{T} = \begin{bmatrix} \mathbf{T}_1 & \mathbf{T}_2 & \mathbf{T}_3 & \mathbf{T}_4 & \mathbf{T}_5 & \mathbf{T}_6 & \mathbf{0}_{1\times n_H} & \mathbf{0}_{1\times n_H} \end{bmatrix}^T$$

$$\mathbf{T}_1 = \left\{ P_{\mathrm{C}q}(r_1), \cdots, P_{\mathrm{C}qk}(r_1), \cdots, P_{\mathrm{C}qn_{\mathrm{H}}}(r_1) \right\}$$

$$\mathbf{T}_2 = \left\{ P_{\mathrm{S}q}(r_1), \cdots, P_{\mathrm{S}qk}(r_1), \cdots, P_{\mathrm{S}qn_{\mathrm{H}}}(r_1) \right\}$$

$$\mathbf{T}_3 = \left\{ P_{\mathrm{C}q}(r_2), \cdots, P_{\mathrm{C}qk}(r_2), \cdots, P_{\mathrm{C}qn_{\mathrm{H}}}(r_2) \right\}$$

$$\mathbf{T}_4 = \left\{ P_{\mathrm{S}q}(r_2), \cdots, P_{\mathrm{S}qk}(r_2), \cdots, P_{\mathrm{S}qn_{\mathrm{H}}}(r_2) \right\}$$

$$\mathbf{T}_5 = \left\{ \frac{\mu_1}{\mu_0}\frac{dP_{\mathrm{C}q}(r)}{dr} - \frac{B_{\mathrm{RC}q}}{\mu_0}, \cdots, \frac{\mu_1}{\mu_0}\frac{dP_{\mathrm{C}qk}(r)}{dr} - \frac{B_{\mathrm{RC}qk}}{\mu_0}, \cdots, \frac{\mu_1}{\mu_0}\frac{dP_{\mathrm{C}qn_{\mathrm{H}}}(r)}{dr} - \frac{B_{\mathrm{RC}qn_{\mathrm{H}}}}{\mu_0} \right\}\Bigg|_{r=r_2}$$

$$\mathbf{T}_6 = \left\{ \frac{\mu_1}{\mu_0}\frac{dP_{\mathrm{S}q}(r)}{dr} - \frac{B_{\mathrm{RS}q}}{\mu_0}, \cdots, \frac{\mu_1}{\mu_0}\frac{dP_{\mathrm{S}qk}(r)}{dr} - \frac{B_{\mathrm{RS}qk}}{\mu_0}, \cdots, \frac{\mu_1}{\mu_0}\frac{dP_{\mathrm{S}qn_{\mathrm{H}}}(r)}{dr} - \frac{B_{\mathrm{RS}qn_{\mathrm{H}}}}{\mu_0} \right\}\Bigg|_{r=r_2}$$

$$\mathbf{Q} = \begin{bmatrix} \mathbf{Q}_1 & \mathbf{Q}_2 & \mathbf{Q}_3 & \mathbf{Q}_4 \end{bmatrix}$$

For $i \leq n_c, k \leq n_{\mathrm{H}}$,

$$\mathbf{Q}_{1\{(i-1)(n_r+1)+1\}\{k\}} = \mu_0 l_a qk r_3^{qk} \int_{\varphi_{i1}}^{\varphi_{i2}} \cos(qk\varphi) d\varphi$$

$$\mathbf{Q}_{2\{(i-1)(n_r+1)+1\}\{k\}} = -\mu_0 l_a qk r_3^{-qk} \int_{\varphi_{i1}}^{\varphi_{i2}} \cos(qk\varphi) d\varphi$$

$$\mathbf{Q}_{3\{(i-1)(n_r+1)+1\}\{k\}} = \mu_0 l_a qk r_3^{qk} \int_{\varphi_{i1}}^{\varphi_{i2}} \sin(qk\varphi) d\varphi$$

$$\mathbf{Q}_{4\{(i-1)(n_r+1)+1\}\{k\}} = -\mu_0 l_a qk r_3^{-qk} \int_{\varphi_{i1}}^{\varphi_{i2}} \sin(qk\varphi) d\varphi$$

$$\mathbf{M} = \begin{bmatrix} \mathbf{M}_1 \\ \mathbf{M}_2 \end{bmatrix}$$

For $i \leq n_c, k \leq n_{\mathrm{H}}$,

$$\mathbf{M}_{1\{k\}\{(i-1)(n_r+1)+1\}} = -\frac{q}{\pi} \int_{\varphi_{i1}}^{\varphi_{i2}} \cos(qk\varphi) d\varphi$$

$$\mathbf{M}_{2\{k\}\{(i-1)(n_r+1)+1\}} = -\frac{q}{\pi} \int_{\varphi_{i1}}^{\varphi_{i2}} \sin(qk\varphi) d\varphi$$

$$\mathbf{K} = \begin{bmatrix} \mathbf{A}_1 & \mathbf{B}_1 & \mathbf{C}_1 & \mathbf{D}_1 & \mathbf{A}_2 & \mathbf{B}_2 & \mathbf{C}_2 & \mathbf{D}_2 \end{bmatrix}$$

$$\mathbf{A}_1 = \left\{ A_{11}, A_{12}, \cdots, A_{1k}, \cdots, A_{1n_{\mathrm{H}}} \right\}^T$$

$$\mathbf{B}_1 = \left\{ B_{11}, B_{12}, \cdots, B_{1k}, \cdots, B_{1n_{\mathrm{H}}} \right\}^T$$

$$\mathbf{C}_1 = \left\{ C_{11}, C_{12}, \cdots, C_{1k}, \cdots, C_{1n_{\mathrm{H}}} \right\}^T$$

$$\mathbf{D}_1 = \left\{D_{11}, D_{12}, \cdots, D_{1k}, \cdots, D_{1n_{\mathrm{H}}}\right\}^T$$
$$\mathbf{A}_2 = \left\{A_{21}, A_{22}, \cdots, A_{2k}, \cdots, A_{2n_{\mathrm{H}}}\right\}^T$$
$$\mathbf{B}_2 = \left\{B_{21}, B_{22}, \cdots, B_{2k}, \cdots, B_{2n_{\mathrm{H}}}\right\}^T$$
$$\mathbf{C}_2 = \left\{C_{21}, C_{22}, \cdots, C_{2k}, \cdots, C_{2n_{\mathrm{H}}}\right\}^T$$
$$\mathbf{D}_2 = \left\{D_{21}, D_{22}, \cdots, D_{2k}, \cdots, D_{2n_{\mathrm{H}}}\right\}^T$$
$$\mathbf{U}_{\mathrm{N}} = \left\{U_1, U_2, \cdots, U_i, \cdots, U_{n_c(n_r+1)}\right\}^T$$

Appendix B

Figure 2 shows the magnetic reluctances in sector-shaped elements. The angle of sector $\Delta\varphi_i(r)$ varies with the value of radius r and can be expressed as follows:

$$\Delta\varphi_i(r) = \frac{\Delta\varphi_i^+ - \Delta\varphi_i^-}{\Delta r_i^+ - \Delta r_i^-}\left(r - r_i^-\right) + \Delta\varphi_i^-.$$

It can be simplified into

$$\Delta\varphi_i(r) = kr + b,$$

in which

$$k = \frac{\Delta\varphi_i^+ - \Delta\varphi_i^-}{\Delta r_i^+ - \Delta r_i^-},$$
$$b = \frac{r_i^+\Delta\varphi_i^- - r_i^-\Delta\varphi_i^+}{r_i^+ - r_i^-}.$$

The whole magnetic reluctance in radial direction $R_{i\mathrm{rad}}$ can be expressed as follows:

$$\begin{aligned}
R_{i\mathrm{rad}} &= \int_{r_i^0}^{r_i^+} \frac{1}{\mu l_a \cdot r \cdot \Delta\varphi_i(r)} dr \\
&= \frac{1}{\mu l_a} \cdot \int_{r_i^-}^{r_+^+} \frac{1}{(kr + b) \cdot r} dr \\
&= \frac{1}{\mu l_a}\left[\frac{1}{b}\ln r - \frac{1}{b}\ln(kr + b)\right]\Bigg|_{r_i^-}^{r_i^+} \\
&= \frac{1}{\mu l_a \cdot b}\ln\frac{r}{\Delta\varphi_i(r)}\Bigg|_{r_i^-}^{r_i^+} \\
&= \frac{\left(r_i^+ - r_i^-\right)}{\mu l_a\left(r_i^+\Delta\varphi_i^- - r_i^-\Delta\varphi_i^+\right)}\ln\left(\frac{r_i^+\Delta\varphi_i^-}{r_i^-\Delta\varphi_i^+}\right).
\end{aligned}$$

The radius of sector R_{i1} varies from r_i^- to r_i^0, and the radius of sector R_{i3} varies from r_i^0 to r_i^+, so the equations of R_{i1} and R_{i3} can be expressed as:

$$R_{i3} = \frac{\left(r_i^+ - r_i^0\right)}{\mu l_a\left(r_i^+\Delta\varphi_i^0 - r_i^0\Delta\varphi_i^+\right)}\ln\left(\frac{r_i^+\Delta\varphi_i^0}{r_i^0\Delta\varphi_i^+}\right),$$

$$R_{i1} = \frac{\left(r_i^0 - r_i^-\right)}{\mu l_a\left(r_i^0\Delta\varphi_i^- - r_i^-\Delta\varphi_i^0\right)}\ln\left(\frac{r_i^0\Delta\varphi_i^-}{r_i^-\Delta\varphi_i^0}\right).$$

In the circumferential direction, the micro-element of the magnetic permeance can be expressed as:

$$d\Lambda = \frac{\mu l_a \cdot dr}{r\Delta\varphi_i(r)}.$$

The whole magnetic permeance $\Lambda_{i\mathrm{circ}}$ is:

$$\begin{aligned}
\Lambda_{i\mathrm{circ}} &= \int_{r_i^-}^{r_i^+} \frac{\mu l_a}{r \cdot (kr+b)} dr \\
&= \mu l_a \left[\frac{1}{b} \ln r - \frac{1}{b} \ln(kr+b) \right] \Big|_{r_i^-}^{r_i^+} \\
&= \mu l_a \frac{1}{b} \ln \frac{r}{\Delta\varphi_i(r)} \Big|_{r_i^-}^{r_i^+} \\
&= \mu l_a \frac{(r_i^+ - r_i^-)}{(r_i^+ \Delta\varphi_i^- - r_i^- \Delta\varphi_i^+)} \ln\left(\frac{r_i^+ \Delta\varphi_i^-}{r_i^- \Delta\varphi_i^+} \right).
\end{aligned}$$

The magnetic reluctances R_{i2} and R_{i4} can, hence, be expressed as follows:

$$R_{i2} = R_{i4} = \frac{1}{2\Lambda_{i\mathrm{circ}}} = \frac{(r_i^+ \Delta\varphi_i^- - r_i^- \Delta\varphi_i^+)}{2\mu l_a (r_i^+ - r_i^-)} \frac{1}{\ln\left(\frac{r_i^+ \Delta\varphi_i^-}{r_i^- \Delta\varphi_i^+} \right)}.$$

References

1. Gao, J.; Dai, L.; Zhang, W. Improved genetic optimization algorithm with subdomain model for multi-objective optimal design of SPMSM. *CES Trans. Electr. Mach. Syst.* **2018**, *2*, 160–165. [CrossRef]
2. Ibala, A.; Rehbi, R.; Masmoudi, A. MEC-Based Modelling of Claw Pole Machines:Application to Automotive and Wind Generating Systems. *Int. J. Renew. Energy Res. IJRER* **2011**, *1*, 110–117 .
3. Rebhi, R.; Ibala, A.; Masmoudi, A. MEC-Based Sizing of a Hybrid-Excited Claw Pole Alternator. *IEEE Trans. Ind. Appl.* **2015**, *51*, 211–223. [CrossRef]
4. Zhang, Z.; Sun, L.; Tao, Y.; Yan, Y. Development of nonlinear magnetic network model of a hybrid excitation doubly salient machine. In Proceedings of the 2013 International Electric Machines & Drives Conference, Chicago, IL, USA, 12–15 May 2013 ; pp. 663–669. [CrossRef]
5. Pfister, P.D.; Yin, X.; Fang, Y. Slotted Permanent-Magnet Machines: General Analytical Model of Magnetic Fields, Torque, Eddy Currents, and Permanent-Magnet Power Losses Including the Diffusion Effect. *IEEE Trans. Magn.* **2016**, *52*, 1–13. [CrossRef]
6. Hannon, B.; Sergeant, P.; Dupré, L.; Pfister, P.D. Two-Dimensional Fourier-Based Modeling of Electric Machines—An Overview. *IEEE Trans. Magn.* **2019**, *55*, 8107217. [CrossRef]
7. Khedda, Z.D.; Boughrara, K.; Dubas, F.; Ibtiouen, R. Nonlinear Analytical Prediction of Magnetic Field and Electromagnetic Performances in Switched Reluctance Machines. *IEEE Trans. Magn.* **2017**, *53*, 8107311. [CrossRef]
8. Dubas, F.; Boughrara, K. New Scientific Contribution on the 2-D Subdomain Technique in Cartesian Coordinates: Taking into Account of Iron Parts. *Math. Comput. Appl.* **2017**, *22*, 17. [CrossRef]
9. Sprangers, R.L.J.; Paulides, J.J.H.; Gysen, B.L.J.; Lomonova, E.A. Magnetic Saturation in Semi-Analytical Harmonic Modeling for Electric Machine Analysis. *IEEE Trans. Magn.* **2016**, *52*, 8100410. [CrossRef]
10. Liu, Z.; Bi, C.; Tan, H.; Low, T.S. A combined numerical and analytical approach for magnetic field analysis of permanent magnet machines. *IEEE Trans. Magn.* **1995**, *31*, 1372–1375. [CrossRef]
11. Laoubi, Y.; Dhifli, M.; Verez, G.; Amara, Y.; Barakat, G. Open Circuit Performance Analysis of a Permanent Magnet Linear Machine Using a New Hybrid Analytical Model. *IEEE Trans. Magn.* **2015**, *51*, 8102304. [CrossRef]
12. Laoubi, Y.; Dhifli, M.; Barakat, G.; Amara, Y. Hybrid analytical modeling of a flux switching permanent magnet machines. In Proceedings of the 2014 International Conference on Electrical Machines (ICEM), Berlin, Germany, 2–5 September 2014; pp. 1018–1023. [CrossRef]
13. Wu, L.J.; Li, Z.; Huang, X.; Zhong, Y.; Fang, Y.; Zhu, Z.Q. A Hybrid Field Model for Open-Circuit Field Prediction in Surface-Mounted PM Machines Considering Saturation. *IEEE Trans. Magn.* **2018**, *54*, 8103812. [CrossRef]
14. Wu, L.J.; Li, Z.K.; Wang, D.; Yin, H.; Huang, X.; Zhu, Z.Q. On-Load Field Prediction of Surface-Mounted PM Machines Considering Nonlinearity Based on Hybrid Field Model. *IEEE Trans. Magn.* **2019**, *55*, 8100911. [CrossRef]
15. Li, Z.; Huang, X.; Wu, L.; Zhang, H.; Shi, T.; Yan, Y.; Shi, B.; Yang, G. An Improved Hybrid Field Model for Calculating On-Load Performance of Interior Permanent-Magnet Motors. *IEEE Trans. Ind. Electron.* **2021**, *68*, 9207–9217. [CrossRef]

16. Tang, C.; Shen, M.; Fang, Y.; Pfister, P.D. Comparison of Subdomain, Complex Permeance, and Relative Permeance Models for a Wide Family of Permanent-Magnet Machines. *IEEE Trans. Magn.* **2021**, *57*, 8101205. [CrossRef]
17. Wu, L.J.; Yin, H.; Wang, D.; Fang, Y. On-Load Field Prediction in SPM Machines by a Subdomain and Magnetic Circuit Hybrid Model. *IEEE Trans. Ind. Electron.* **2020**, *67*, 7190–7201. [CrossRef]
18. Yin, H.; Wu, L.; Zheng, Y.; Fang, Y. Magnetic Field Prediction in Surface-Mounted PM Machines with Parallel Slot Based on a Nonlinear Subdomain and Magnetic Circuit Hybrid Model. In Proceedings of the 2019 IEEE International Electric Machines & Drives Conference (IEMDC), San Diego, CA, USA, 12–15 May 2019; pp. 1427–1432. [CrossRef]
19. Zhu, Y.; Liu, G.; Xu, L.; Zhao, W.; Cao, D. A Hybrid Analytical Model for Permanent Magnet Vernier Machines Considering Saturation Effect. *IEEE Trans. Ind. Electron.* **2022**, *69*, 1211–1223. [CrossRef]
20. Chikouche, B.L.; Boughrara, K.; Dubas, F.; Ibtiouen, R. Analytical magnetic field calculation for flat permanent-magnet linear machines with dual-rotor by using improved two-dimensional hybrid analytical method. *COMPEL-Int. J. Comput. Math. Electr. Electron. Eng.* **2021**, *40*, 602–623. [CrossRef]
21. Ouagued, S.; Amara, Y.; Barakat, G. Cogging Force Analysis of Linear Permanent Magnet Machines Using a Hybrid Analytical Model. *IEEE Trans. Magn.* **2016**, *52*, 8202704. [CrossRef]
22. Ouagued, S.; Amara, Y.; Barakat, G. Comparison of hybrid analytical modelling and reluctance network modelling for pre-design purposes. *Math. Comput. Simul.* **2016**, *130*, 3–21. [CrossRef]
23. Zhu, Z.Q.; Wu, L.J.; Xia, Z.P. An Accurate Subdomain Model for Magnetic Field Computation in Slotted Surface-Mounted Permanent-Magnet Machines. *IEEE Trans. Magn.* **2010**, *46*, 1100–1115. [CrossRef]
24. Zhu, Z.; Howe, D.; Bolte, E.; Ackermann, B. Instantaneous magnetic field distribution in brushless permanent-magnet DC motors. I. Open-circuit field. *IEEE Trans. Magn.* **1993**, *29*, 124–135. [CrossRef]